



**HAL**  
open science

# The Electrical Conductivity of Liebermannite: Implications for Water Transport Into the Earth's Lower Mantle

Geeth Manthilake, Federica Schiavi, Chengcheng Zhao, Mainak Mookherjee,  
Mohamed Ali M.A. Bouhifd, Laurent Jouffret

► **To cite this version:**

Geeth Manthilake, Federica Schiavi, Chengcheng Zhao, Mainak Mookherjee, Mohamed Ali M.A. Bouhifd, et al.. The Electrical Conductivity of Liebermannite: Implications for Water Transport Into the Earth's Lower Mantle. *Journal of Geophysical Research: Solid Earth*, 2020, 125 (8), 10.1029/2020JB020094 . hal-02933235

**HAL Id: hal-02933235**

**<https://uca.hal.science/hal-02933235>**

Submitted on 26 Nov 2020

**HAL** is a multi-disciplinary open access archive for the deposit and dissemination of scientific research documents, whether they are published or not. The documents may come from teaching and research institutions in France or abroad, or from public or private research centers.

L'archive ouverte pluridisciplinaire **HAL**, est destinée au dépôt et à la diffusion de documents scientifiques de niveau recherche, publiés ou non, émanant des établissements d'enseignement et de recherche français ou étrangers, des laboratoires publics ou privés.



Distributed under a Creative Commons Attribution 4.0 International License

1 **The electrical conductivity of liebermannite: Implications for water transport into the**  
2 **Earth's lower mantle**

3  
4  
5 Geeth Manthilake<sup>1\*</sup>, Federica Schiavi<sup>1</sup>, Chengcheng Zhao<sup>1</sup>, Mainak Mookherjee<sup>2</sup>, Mohamed Ali  
6 Bouhifd<sup>1</sup>, Laurent Jouffret<sup>3</sup>

7  
8 <sup>1</sup> Laboratoire Magmas et Volcans, CNRS, IRD, OPGC, Université Clermont Auvergne,  
9 63000 Clermont-Ferrand, France

10 <sup>2</sup> Earth Materials Laboratory, Department of Earth, Ocean and Atmospheric Sciences, Florida State  
11 University, Tallahassee, FL, 32306, USA

12 <sup>3</sup> Laboratoire des Matériaux et du Génie Physique, UMR 5628, 3 parvis Louis Néel - CS50257 -  
13 38016 Grenoble, France

14  
15 **\*Corresponding author:** Geeth Manthilake ([geeth.manthilake@uca.fr](mailto:geeth.manthilake@uca.fr))

16  
17  
18 **Key Points:**

- 19 • The hopping of K<sup>+</sup> ions in liebermannite results in high electrical conductivity of more  
20 than 1 S/m.
- 21 • Water can be present as both molecular H<sub>2</sub>O and hydroxyl (OH<sup>-</sup>) groups in liebermannite
- 22 • High H<sub>2</sub>O contents of ocean island basalts can be related to deeply subducted hydrous  
23 liebermannite

25 **Abstract**

26           Liebermannite ( $\text{KAlSi}_3\text{O}_8$ ) is a principal mineral phase expected to be thermodynamically  
27 stable in deeply subducted continental and oceanic crusts. The crystal structure of liebermannite  
28 exhibits tunnels that are formed between the assemblies of double chains of edge-sharing (Si, Al)  
29  $\text{O}_6$  octahedral units, which act as a repository for large incompatible alkali ions. In this study, we  
30 investigate the electrical conductivity of liebermannite at 12, 15, and 24 GPa and temperature of  
31 1500 K to track subduction pathways of continental sediments into the Earth's lower mantle.  
32 Further, we looked at whether liebermannite could sequester incompatible  $\text{H}_2\text{O}$  at deep mantle  
33 conditions. We observe that the superionic conductivity of liebermannite due to the thermally  
34 activated hopping of  $\text{K}^+$  ions results in high electrical conductivity of more than 1 S/m. Infrared  
35 spectral features of hydrous liebermannite indicate the presence of both molecular  $\text{H}_2\text{O}$  and  
36 hydroxyl ( $\text{OH}^-$ ) groups in its crystal structure. The observed high electrical conductivity in the  
37 mantle transition zone beneath Northeastern China and the lower mantle beneath the Philippine  
38 Sea can be attributed to the subduction pathways of continental sediments deep into the Earth's  
39 mantle. While major mineral phases in pyrolitic compositions are almost devoid of  $\text{H}_2\text{O}$  under  
40 lower mantle conditions, our study demonstrates that liebermannite could be an important host of  
41  $\text{H}_2\text{O}$  in these conditions. We propose that the relatively high  $\text{H}_2\text{O}$  contents of ocean island basalts  
42 derived from deep mantle plumes are primarily related to deeply subducted continental sediments,  
43 in which liebermannite is the principal  $\text{H}_2\text{O}$  carrier.

44

45

46

47

48

49

50 **Plain Language Summary**  
51

52           Liebermannite ( $\text{KAlSi}_3\text{O}_8$ , formally K-hollandite) is an important mineral phase in deeply  
53 subducted continental and oceanic crusts. Liebermannite exhibits high ionic conductivity and  
54 could explain low resistivity in the Earth's mantle transition zone and the upper part of the lower  
55 mantle, hinting towards the subduction of hydrated crusts into the lower mantle. The liebermannite  
56 samples synthesized at these conditions indicate the presence of both molecular  $\text{H}_2\text{O}$  and hydroxyl  
57 ( $\text{OH}^-$ ) groups in its crystal structure, suggesting that liebermannite could be an important host of  
58  $\text{H}_2\text{O}$  in the Earth's deep mantle. Compared to the basalts from mid-ocean ridges that exhibit trace  
59 quantities of water, ocean island basalts show higher water contents. It has been speculated that  
60 ocean basalts are derived from crustal components that were deeply subducted. It is also known  
61 that the lower mantle is relatively dry. Therefore, it is difficult to reconcile the higher water  
62 contents in OIBs that are derived from the deep mantle. Here, we demonstrate that the source  
63 crustal components for OIBs were likely to be hydrated. Liebermannite is a key mineral in deeply  
64 subducted crusts and can efficiently host water.

65  
66  
67  
68  
69  
70  
71  
72  
73  
74  
75  
76

**77 1. Introduction**

78 Trace quantities of H<sub>2</sub>O stored in the Earth's mantle significantly influence the physical  
79 properties of mantle rocks (Smyth & Jacobsen, 2006). Although H<sub>2</sub>O plays an important role by  
80 affecting both mineral properties and mantle dynamics of the upper mantle, it is well known that  
81 the Earth's lower mantle is relatively dry, as indicated by the low (< 1000 ppm wt.) H<sub>2</sub>O solubility  
82 in major lower mantle mineral phases (Bolfan-Casanova et al., 2003; Fu et al., 2019; Hirschmann,  
83 2006). Yet some oceanic island basalts (OIB), which are characterized by relatively high H<sub>2</sub>O  
84 contents up to ~ 2.0 wt. %, are fed by plumes rising from the lower mantle (Deschamps et al.,  
85 2011). These plumes are thought to originate from enriched reservoirs composed of recycled  
86 crustal materials that subducted into the deep mantle (Willbold & Stracke, 2006). Hydrous phases  
87 associated with subducting slabs descending into the lower mantle (van der Hilst et al., 1997) may  
88 provide a plausible mechanism for transporting H<sub>2</sub>O into the deep mantle. Dense hydrous  
89 magnesium silicates (DHMS), such as phase H and phase D, which are known to be stable in the  
90 depleted portion of the subducting slab at lower mantle conditions, are likely to transport H<sub>2</sub>O into  
91 the lower mantle and subsequently hydrate the subducted crustal components (Nishi et al., 2014;  
92 Pamato et al., 2014).

93 While the dominant component of all OIB is likely to be recycled basaltic oceanic crust,  
94 both chemical and isotopic signatures of OIB indicate the mixing of different source materials  
95 (Hart, 1988). Particularly the Enriched Mantle II (EMII)-type OIB, which have been found in the  
96 Society Islands, the Marquesas and Samoa, suggest a 5-10 % of continental and sedimentary  
97 components (Hart, 1988). Water contents up to 1.5 wt. % and low H<sub>2</sub>O/Ce (<150) have been  
98 reported in such EMI type OIB (Cabral et al., 2014). The estimates based on geochemical  
99 analyses indicate that H<sub>2</sub>O concentrations in EMI sources are about 400 ppm wt. (Dixon et al.,

100 2002). The low H<sub>2</sub>O/Ce measured in EM-type magmas indicates up to 92 % H<sub>2</sub>O loss from the  
101 recycled continental components with progressive dehydration (Dixon et al., 2002). Despite  
102 intense dehydration, the deeply subducted slab appears to retain or rehydrate by the dehydration  
103 of dense hydrous phases such that a sufficient amount of H<sub>2</sub>O is available in the deep OIB sources  
104 (Dixon et al., 2002).

105 Liebermannite, formerly known as Liebermannite, is the high-pressure polymorph of  
106 KAlSi<sub>3</sub>O<sub>8</sub>-feldspar and is likely to be stable in deeply subducted (> 300 km) continental crust and  
107 mid-oceanic ridge basalt compositions enriched in potassium (Schmidt, 1996). The crystal  
108 structure of liebermannite exhibits tunnels that are formed between the assemblies of double chains  
109 of edge-sharing (Si, Al)O<sub>6</sub> octahedral units. At pressures ≤ 20-23 GPa, liebermannite (*lowP*)  
110 crystallizes in a tetragonal (*I4/m*) space group symmetry, whereas above these pressures, the  
111 tunnels are slightly squeezed, and the high-pressure polymorph of liebermannite (*hiP*) crystallizes  
112 in a monoclinic (*I2/m*) space group symmetry (Ferroir et al., 2006; Nishiyama et al., 2005). These  
113 tunnels accommodate incompatible cations such as Na, K, Sr, Ba, La, and Pb. A naturally  
114 occurring liebermannite containing Ba<sup>2+</sup> and K<sup>+</sup> is reported to contain up to 5 wt. % H<sub>2</sub>O in its  
115 crystal structure (Miura, 1986), indicating that liebermannite could be an important host for H<sub>2</sub>O.  
116 The *hiP* polymorph is observed to be stable down to the Earth's lowermost mantle conditions  
117 (Kawai & Tsuchiya, 2013; Sueda et al., 2004). At mantle transition zone conditions, phase  
118 equilibria studies indicate that average continental crust is composed of a mixture of liebermannite  
119 (~32 vol. %), stishovite (24 vol.%), majoritic garnet (30 vol. %) and minor amounts of calcium  
120 aluminosilicate (CAS) phases (Irifune et al., 1994).

121 The presence of tunnels in the crystal structure of liebermannite facilitates the motion of  
122 K<sup>+</sup> ions along the channel, attaining superionic conduction at high temperatures (Furusawa et al.,

123 1988; Khanna et al., 1981; Yoshikado et al., 1982). More recently, the electrical conductivity of  
124 liebermannite, relevant for the deeply subducted crust, has been examined using molecular  
125 dynamics simulations. The predicted electrical conductivity for liebermannite with a 12.5 %  
126 vacancy in the tunnel is ~20 S/m at 10 GPa and 1600 K (He et al., 2016). The magnitude of the  
127 predicted electrical conductivity resulting from ionic conduction of  $K^+$  ions in the tunnels is  
128 significantly greater than that of the electrical conductivity due to extrinsic defects. Hence, owing  
129 to its high electrical conductivity, liebermannite potentially represents an ideal tracer mineral for  
130 tracking subducted pathways of continental crustal components into the Earth's lower mantle.

131         The unique crystal structure of liebermannite and the ability to accommodate large alkali  
132 ions and possibly  $H_2O$  in its tunnels highlight its importance as a possible  $H_2O$  repository in the  
133 subducted crustal components and a possible source for OIB. However, so far, studies on  
134 liebermannite have been restricted to the equation of state, elasticity (Caracas & Boffa Ballaran,  
135 2010; Kawai & Tsuchiya, 2013; Mookherjee & Steinle-Neumann, 2009), and electrical  
136 conductivity (He et al., 2016) of the dry variety.

137         In this study, we first conducted high-pressure and temperature experiments to constrain  
138 the electrical conductivity of hydrous liebermannite at the upper mantle, transition zone, and lower  
139 mantle conditions, i.e., at pressures of 12, 15, and 24 GPa respectively. Then we examined the  
140 water incorporation mechanisms in liebermannite. Finally, we explore whether the high  $H_2O$   
141 contents of OIB could have derived from hydrated crustal components of deeply subducted slabs  
142 penetrated down to the lower mantle.

143

144

145

## 146 **2. Materials and Methods**

147 The starting powder was prepared using high purity oxide mixtures of  $\text{K}_2\text{CO}_3$ ,  $\text{Al}_2\text{O}_3$ , and  
148  $\text{SiO}_2$ . The mixture was slowly heated to 1000 °C overnight in a platinum crucible for decarbonate  
149  $\text{K}_2\text{CO}_3$ . The decarbonated powdered mixture was then heated to 1500 °C and kept 10 minutes to  
150 obtain homogeneous glass. The time was optimized to avoid possible K loss at high temperatures.

151 High pressure-high temperature experiments were conducted using a 1500-ton multi-anvil  
152 apparatus. The pre-synthesis of K-feldspar for electrical conductivity measurements were  
153 conducted at 2 GPa and 1200 K in a 14/8 assembly (Fig. 1a). To synthesize hydrous K-feldspar we  
154 add  $\text{Al}(\text{OH})_3$  to the glass mixture to obtain ~ 100 wt. ppm  $\text{H}_2\text{O}$ . The powdered mixture was packed  
155 into a capsule made of rhenium (Re), and kept at high-pressure and high-temperature for durations  
156 of 4 hours to obtain the cylindrical samples for electrical conductivity measurements. The water  
157 contents of K-feldspar is measured to be  $257 \pm 29$  wt. ppm.

158 The pressure and temperature conditions for the electrical conductivity measurements were  
159 carefully chosen based on the stability of liebermannite (Nishiyama et al., 2005) and represent the  
160 upper mantle (12 GPa), mantle transition zone (15 GPa), and the upper part of the lower mantle  
161 (24 GPa). Electrical conductivity measurements were performed using octahedral pressure  
162 medium composed of MgO and  $\text{Cr}_2\text{O}_3$  (5 wt. %) in a 14/8 assembly (octahedron edge length/anvil  
163 truncation edge length) at 12 GPa, in a 14/6 assembly at 15 GPa, and a 10/4 assembly at 24 GPa  
164 (Fig.1b). MgO ceramic sleeves insulated the electrode wires from the furnace. All ceramic  
165 assembly parts, including the pressure media, were baked at 1000 °C for more than 12 hours and  
166 then stored at 125 °C in high-vacuum furnaces (< 100 mTorr) before assembling. This step  
167 reduces the exposure of assembly components to atmospheric moisture and other impurities. The  
168 sample temperature was measured using a type-C tungsten-rhenium (W95Re5-W74Re26)

169 thermocouple junction, placed at one end of the sample. One cable formed the thermocouple and  
170 a separate W<sub>95</sub>Re<sub>5</sub> cable placed at the opposite side of the sample connected to the impedance  
171 spectroscopy for the electrical conductivity measurements.

172 The electrical conductivity of liebermannite samples was determined using the impedance  
173 spectroscopy method using the Modulab MTS Impedance gain-phase analyzer. The frequency  
174 range for the analyses was 10<sup>6</sup>-10<sup>1</sup> Hz. After compressing the assembly to the desired pressure,  
175 samples were heated to 500 K and while maintaining a temperature of 500 K, the electrical  
176 resistance of the sample was measured regularly until the sample resistance reached a stable value.  
177 The decrease of electrical resistance observed at this step corresponds to the removal of the  
178 absorbed moisture in the sample capsule and the surrounding area, which could be incorporated  
179 into the sample at higher temperatures (Manthilake et al., 2015). During the measurements, sample  
180 resistance was determined in several heating and cooling cycles until the electrical resistance of  
181 heating and cooling paths become reproducible. For the discussion, we have used the data from  
182 the last cooling cycle, which minimizes the uncertainty in electrical conductivity. The sample  
183 resistance can be obtained by fitting the impedance spectra with an appropriate equivalent circuit.  
184 For polycrystalline samples, as we use in this study, the equivalent circuit can be illustrated by a  
185 combination of resistor-capacitor/constant phase element (R-C/CPE) components, connected in  
186 parallel, series, or a series-parallel combination. Once the electrical resistivity of the samples was  
187 determined from the fit of the impedance spectra, the electrical conductivity was determined using  
188 the radius and the axial length of the cylindrical sample measured after each experiment. The  
189 inherent assumption is that the sample geometry remained constant during the experiment.

190 The chemical compositions the experimental run products were investigated using a  
191 Cameca SxFiveTactis electron probe microanalyzer (EPMA) in wavelength dispersive (WDS)

192 mode operating at an accelerating voltage of 15 kV and 4 nA beam current. The low accelerating  
193 voltage was used to avoid the K loss in liebermannite.

194 Powder X-ray diffraction (PXRD) analyses of experimental run products were carried out  
195 to identify the crystal structures of liebermannite and the phases present in quenched samples at  
196 15 and 24 GPa. The PXRD was obtained for  $\sim 1 \text{ mm}^3$  of crushed samples that were placed on zero-  
197 background Si sample holders. The PXRD was recorded using a Philipps X-Pert Pro diffractometer  
198 with  $\text{CuK}\alpha$  radiation source ( $\lambda = 0.15405 \text{ nm}$ ). The PXRD patterns were recorded over the  $10\text{--}90^\circ$   
199 ( $2\theta$ ) range in steps of  $0.0167^\circ$  with a counting time of 700 s per step. Lattice parameters were  
200 obtained from LeBail fits using the FULLPROF program (Rodriguez-Carvajal, 1993). The  
201 background can be obtained by linear interpolation between twenty-six points, and the peak  
202 profiles were modeled using a pseudo-Voigt function.

203 Raman spectroscopy was used to identify liebermannite and the minor mineral phases  
204 present in the experimental run products. Raman spectra were collected in a back-scattered  
205 geometry using an InVia confocal Raman micro-spectrometer, equipped with a 532 nm diode laser,  
206 a Peltier-cooled CCD detector, a Rayleigh rejection edge filter (Schiavi et al., 2018). The laser  
207 power of 1-8 mW; the slit aperture of  $65 \mu\text{m}$ , and a grating of 2400 l/mm were used for the present  
208 analyses. These conditions result in lateral and axial spatial resolutions of  $\sim 1$  and  $3 \mu\text{m}$  and a  
209 spectral resolution of  $1 \text{ cm}^{-1}$ . Acquisition times were 30-60 s and 60-240 s for the low-wavenumber  
210 and high-wavenumber region, respectively.

211 The quantification of  $\text{H}_2\text{O}$  in liebermannite was performed using the Fourier Transform  
212 Infrared (FTIR) spectroscopy. Unpolarized FTIR spectra of liebermannite were acquired using a  
213 Vertex70 Bruker spectrometer equipped with a Globar light source, a KBr beamsplitter, and an  
214 MCT (Mercury-Cadmium-Tellurium alloy) detector. The beam size for the analyses was  $\sim 30 \mu\text{m}$ .

215 The spectra were obtained through a CaF<sub>2</sub> window with a resolution of 4 cm<sup>-1</sup>. About 2000 scans  
 216 were accumulated for a single spectrum. Thin slabs were cut perpendicular to the compression axis  
 217 of the experimental run products using a high-precision diamond wire saw and polished using  
 218 diamond mats without acetone or bond materials, such as crystal-bond or orthodontic adhesive  
 219 paste to avoid IR signal contaminations. Being the samples polycrystalline, it was not possible to  
 220 perform polarized measurements on single crystals; therefore, we estimated the H<sub>2</sub>O content of  
 221 each sample based on several spectra that were taken over many randomly oriented crystals. The  
 222 spectra were integrated between 2600 and 3800 cm<sup>-1</sup>, an average of several spectra was calculated  
 223 for each sample and multiplied by a factor 3. The OH content was quantified using the Beer-  
 224 Lambert law:

$$225 \quad C_{\text{H}_2\text{O}} = 18.02 \times A \times 10^6 / \varepsilon \times t \times \rho$$

226 where C<sub>H<sub>2</sub>O</sub> is the concentration of hydrous species expressed in ppm H<sub>2</sub>O by weight, 18.02 is the  
 227 molecular weight of H<sub>2</sub>O; A is the total integrated area of bands in the region of interest, *t* is the  
 228 thickness of the sample in cm,  $\varepsilon$  is the molar absorption coefficient, and  $\rho$  is the density of the  
 229 sample in g/L. For the estimation of H<sub>2</sub>O content in liebermannite, we used the theoretically  
 230 predicted integral molar absorption coefficient of 250000 L/(mol.cm<sup>2</sup>) (Koch-Müller & Rhede,  
 231 2010).

232

### 233 **3. Results**

234 The electrical conductivity of liebermannite samples at 12, 15, and 24 GPa are summarized  
 235 in **Fig. 2**. The discontinuous increase in electrical conductivity at a temperature above 660 K during  
 236 the first heating cycle of the 12 GPa experiment coincides with the transformation of K-Feldspar  
 237 to liebermannite with increasing temperature (**Fig. 2a**). This transformation accounts for more than

238 one order of magnitude increase of conductivity for liebermannite. After the complete  
239 transformation, the electrical conductivity of liebermannite increases with increasing temperature  
240 from 700 K to 1500 K and reached to about 1 S/m at 12 GPa and 1500 K. The increase of pressure  
241 appears to have an inverse effect on the electrical conduction in liebermannite (**Fig. 2b**). The  
242 impedance spectra of the sample undergoing K-feldspar to liebermannite transition with increasing  
243 temperature are shown (**Fig. 3**).

244 The activation enthalpy ( $\Delta H$ ) of each conduction mechanism can be calculated by fitting  
245 the data to equation,  $\sigma = \sigma_0 \exp(-\Delta H/RT)$ , where  $\sigma$  is the electrical conductivity (S/m), T is the  
246 absolute temperature (K),  $\sigma_0$  is the pre-exponential factor (S/m), and R is the gas constant (J/K  
247 mol). Here, we analyzed the activation enthalpy, first by manually fitting different temperature  
248 segments to the fitting equation and, second, by fitting the equation to the entire temperature range  
249 (Fei et al., 2020). The estimated activation enthalpies for different conduction mechanisms obtained  
250 using two fitting methods are listed in **Table 1**.

251 The EPMA, SEM, and Raman grid-analyses indicate that liebermannite is the principal  
252 phase present in samples synthesized at 12, 15, and 24 GPa (**Fig. 4**). However, minor amounts of  
253 wadeite, kyanite, and stishovite presence in our samples, an observation consistent with a previous  
254 study (Urakawa et al., 1994) (**Table. 2**) (**Fig.5**). The grid analyses with a step size of 5  $\mu\text{m}$  also  
255 confirmed the absence of melt in our samples. The minor phases mostly occur as isolated grains  
256 within the liebermannite matrix (**Fig 5a**) and the volume fraction of minor phases appeared to  
257 decrease with increasing pressure. Chemical analyses of minor phases at the 24 GPa sample were  
258 hampered by either absence of minor phases (e.g kyanite) at high-pressure samples or if present,  
259 their extremely small grain sizes ( $< 5\mu\text{m}$ ).

260 The FTIR analyses of liebermannite samples after the electrical conductivity measurements  
261 indicate water contents of  $1044\pm 87$  wt. ppm at 12 GPa,  $885\pm 78$  wt. ppm at 15 GPa and  $1104\pm 18$   
262 wt. ppm at 24 GPa (**Fig 6**). The high water contents compared to the K-feldspar starting material  
263 suggest that the absorbed moisture in the assembly parts may have been incorporated into the  
264 sample during the K-feldspar-liebermannite transformation at high-temperature, yielding high  
265 water contents in the liebermannite samples (i.e. higher than the amount of water produced by the  
266 decomposition of  $\text{Al}(\text{OH})_3$ ). We were not able to produce water-free liebermannite samples even  
267 with dry pressure materials.

268 The infrared spectra provide information on water incorporation in liebermannite (**Fig. 6**).  
269 Several O-H vibrational modes are observed: (1) the stretching vibrations of weakly hydrogen  
270 bound hydroxyl units produce intense bands between  $3700$  and  $3500\text{ cm}^{-1}$ ; these modes are more  
271 pronounced in the 12 GPa sample. (2) The stretching vibrations of both  $\text{H}_2\text{O}$  molecules and more  
272 strongly hydrogen bound hydroxyl units occur in the  $3425$ - $3100\text{ cm}^{-1}$  wavenumber range; they  
273 become dominant in the 15 and 24 GPa samples (**Fig. 6a**). (3) The O-H stretching and bending  
274 vibrations of the hydronium ( $\text{H}_3\text{O}^+$ ) ion are observed near  $2900\text{ cm}^{-1}$  and  $1665\text{ cm}^{-1}$ ; these modes  
275 disappear at the highest pressure. In the absence of organic contaminants, such as acetone or bond  
276 materials, the coexistence of these two modes confirms the presence of  $\text{H}_3\text{O}^+$  in *lowP*  
277 liebermannite. (4) The H-O-H bending vibration of the water molecule slightly shifts from  $1610$   
278 to  $1630\text{ cm}^{-1}$  with increasing pressure (**Fig. 6b**). (5) The combination (stretching/bending) modes  
279 of both  $\text{H}_2\text{O}$  molecules (near  $5200\text{ cm}^{-1}$ ) and hydroxyl units (near  $4500\text{ cm}^{-1}$ ) display continuous  
280 shift to lower frequencies with increasing pressure (**Fig. 6c**). This shift is compatible with the  
281 increase of the strength of hydrogen bonds with pressure, as usually observed in minerals (Cynn  
282 & Hofmeister, 1994). The observed spectral features suggest the presence of  $\text{H}_2\text{O}$  and  $\text{H}_3\text{O}^+$

283 substituting for  $K^+$  in the tunnel (Bethell & Sheppard, 1953) and the substitution of hydrogen ( $H^+$ )  
284 in octahedral sites where it forms O-H bonds with one of the six possible oxygen ions in the vacant  
285 octahedral site.

286 The powder X-ray diffraction analyses were conducted on the samples synthesized at 15  
287 GPa and 24 GPa. Both patterns can be refined with parameters consistent with the  $I4/m$  phase:  
288  $a = 9.3304(4)\text{\AA}$ ,  $c = 2.7223(2)\text{\AA}$ . Obtaining the same lattice parameters for the samples out of the  
289 different pressures of annealing experiments implies that the liebermannite phase is elastic enough  
290 to regain its low-pressure parameters consistent with previous studies (Nishiyama et al., 2005;  
291 Sueda et al., 2004).

292

## 293 **4. Discussion and conclusions**

### 294 **4.1 Electrical conduction in liebermannite**

295 The electrical conductivity of K-feldspar before transforming into liebermannite exhibit  
296 higher electrical conductivity compared to the previous electrical conductivity measurements of  
297 F-feldspar reported at 1 GPa (Hu et al., 2013). The high electrical conductivity of K-feldspar  
298 observed in our study can be explained by the 0.02 wt. %  $H_2O$  contents in our samples, compared  
299 to the dry verity reported by Hu et al. 2013 study. Similar electrical behavior has been observed in  
300 dry albite and water-bearing albite (Hu et al., 2013; Ni et al., 2011).

301 The electrical conductivity of hydrous liebermannite increases discontinuously upon  
302 increasing temperature (**Fig. 2b**). At temperatures below 700 K, conductivity is likely to be  
303 dominated by molecular water that is loosely bound in the tunnel sites and the associated activation  
304 energy is less than 0.40 eV. In the temperature range between 700 K and 1100 K, the conductivity  
305 is likely largely due to extrinsic proton defects that are formed due to coupled substitutions of the

306 octahedral sites. The associated activation energy varies between 0.64 eV and 0.78 eV. At  
307 temperatures above 1200 K, the conductivity is likely to be dominated by fast motions of  $K^+$  or  $H^+$   
308 ions (from  $H_3O^+$ ) ions in the channel. The associated activation energy is greater than 0.82 eV.  
309 Higher conductivity has also been observed in alkali bearing materials with the hollandite crystal  
310 structure (Khanna et al., 1981). Such higher conductivity is often referred to as super-ionic  
311 conductivity (He et al., 2016; Khanna et al., 1981). In our study, we are documenting such effects  
312 at extreme pressures of 12 to 24 GPa in liebermannite.

313         The electrical conductivity of minor phases, wadeite, stishovite, and kyanite should not  
314 interfere with the measured conductivity of liebermannite due to their low volume fractions (occur  
315 as isolated grains). Based on chemical analyses of individual liebermannite grains in our samples,  
316 we observe a maximum of 7 %  $K^+$  site vacancy in our liebermannite after electrical conductivity  
317 measurements at 12, 15, and 24 GPa. The intrinsic defects seem to dominate the conduction  
318 mechanism at high temperatures, whereas extrinsic defects may be responsible for the observed  
319 conductivity at lower temperatures.

320

#### 321 **4.2 Water incorporation in liebermannite**

322         The occurrence of several OH stretching bands (Fig. 4a) suggests that different substitution  
323 mechanisms take place, including  $H^+$  substitution in octahedral sites and  $H_2O/H_3O^+$  in tunnels,  
324 resulting in distinct hydrogen bonding strengths. Protons attachment to both bridging and non-  
325 bridging oxygen can also help to explain such a wide range of OH stretching vibrations. Strong  
326 pleochroism in the  $3500\text{-}3600\text{ cm}^{-1}$  range of the polycrystalline sample at 12 GPa indicates the  
327 random orientation of the crystals, in contrast to higher pressure samples. Water/hydrogen could  
328 be incorporated in liebermannite structure in a variety of sites including the substitution of  $H^+$  in

329 the silicon octahedral sites, i.e.,  $\text{Si}_{\text{Si}}^{4+} = \text{Al}_{\text{Si}}^{3+} + \text{H}_{\text{Si}}^{1+}$  or  $\text{Si}_{\text{Si}}^{4+} = 4\text{H}_{\text{Si}}^{1+}$ , the substitution of  $\text{H}^+$  in the  
 330 aluminum octahedral site  $\text{Al}_{\text{Al}}^{3+} = 3\text{H}_{\text{Al}}^{1+}$ , the substitution of  $\text{H}^+$  and  $\text{H}_3\text{O}^+$  in the potassium site  
 331 ( $\text{K}_{\text{K}}^{1+} = \text{H}_{\text{K}}^{1+}$ , or  $\text{K}_{\text{K}}^{1+} = (\text{H}_3\text{O})_{\text{K}}^{1+}$ ) and accommodation of molecular  $\text{H}_2\text{O}$  in the tunnel as in  
 332  $\text{KAlSi}_3\text{O}_8 + \text{H}_2\text{O} = \text{KAlSi}_3\text{O}_8 \cdot \text{H}_2\text{O}$ . The chemical analyses provide crucial information on possible  
 333 coupled substitution mechanisms for hydrogen incorporation in liebermannite. The slight  
 334 deficiency in silicon and increase in aluminum observed in some liebermannite grains  
 335 ( $\text{K}_{0.957 \pm 0.044} \text{Al}_{1.090 \pm 0.057} \text{Si}_{2.931 \pm 0.032} \text{O}_8$ ) is consistent with a reaction involving a substitution in the  
 336 distorted octahedral with the direct replacement of  $\text{Si}^{4+}$  by  $\text{Al}^{3+}$  and  $\text{H}^+$  or by  $4\text{H}^+$ . The chemical  
 337 analyses also indicate a slight aluminum deficiency in some crystals ( $\text{K}_{1.00} \text{Al}_{0.983} \text{Si}_{3.01} \text{O}_8$ ). This  
 338 may suggest possible proton substitution in the octahedral site, replacing  $\text{Al}^{3+}$  with  $3\text{H}^+$ .

339 As the *hiP* liebermannite is considered the dominant polymorph throughout the Earth's  
 340 lower mantle, knowledge on water solubility in the *hiP* structure becomes crucial to assess the  
 341 transport of  $\text{H}_2\text{O}$  to the deepest lower mantle regions through deep extending slabs. Given the  
 342 positive clapeyron slope of  $P$  (GPa) =  $16.6 + 0.007 K$  (T) between the *lowP* and *hiP* liebermannite  
 343 and assuming that trace quantity of water is unlikely to affect the slope, the hydrous liebermannite  
 344 sample synthesized at 24 GPa and 1500 K is expected to be the *lowP* polymorph with tetragonal  
 345 symmetry (Nishiyama et al., 2005). However, upon a decrease of temperature to 1000 K, at  
 346 constant pressure, the sample is likely to transform to *hiP* liebermannite with monoclinic symmetry  
 347 (Nishiyama et al., 2005). Upon structural transformation from *lowP* to *hiP* liebermannite, the  
 348 electrical resistivity measurements of the sample do not indicate a discontinuous decrease of the  
 349 electrical resistance, which indicates the release of free fluid phase or hydrous melting in the  
 350 sample (Freitas & Manthilake, 2019). Assuming that the water incorporation into the liebermannite  
 351 structure occurs at the highest temperature, this crucial observation suggests that the *hiP*

352 liebermannite structure is capable of sequestering  $H^+$  into octahedral sites as molecular  $H_2O$  or  
353 ionic  $H_3O^+$  in its structure similar to the *lowP* liebermannite. The incorporation of  $H_2O$  has been  
354 observed in both naturally occurring tetragonal and monoclinic hollandite crystal structures with  
355 different stoichiometry (Miura, 1986), thus confirming our observations on liebermannite. The  
356 micro Raman grid-analyses of our samples after electrical conductivity measurements indicate the  
357 absence of melt phases, confirming that the water expulsion may not occur in our samples at high  
358 temperatures.

359         Due to the small grain sizes ( $< 5 \mu m$ ), infrared analyses in these minor phases were not  
360 possible; nevertheless, absence of peaks in the high-wavenumber region of the Raman spectra of  
361 wadeite and Al-free stishovite indicates that water is not present within their crystal structure (**Fig.**  
362 **7**). However,  $H_2O$  contents up to 3 wt. % have been observed in stishovite containing aluminum  
363 (Litasov et al., 2007; Yoshino et al., 2014). IR spectral features of Al-free stishovite exhibit some  
364 similarities with those of liebermannite in the spectral range from 3111 to 3261 (Litasov et al.,  
365 2007). Particularly peak position of  $3117 \text{ cm}^{-1}$  in the sample synthesized at 15 GPa (**Fig. 7a**)  
366 overlaps the main peak position of stishovite at  $3117 \text{ cm}^{-1}$  observed for Al- free and Al-bearing  
367 stishovite (Yoshino et al., 2014). In order to confirm that the spectral feature at  $3117 \text{ cm}^{-1}$  in  
368 liebermannite, we have analyzed the O-H region of the Raman spectra of stishovite in the 15 GPa  
369 sample. The observed water-free conditions (**Fig 7a**) strongly suggests the spectral feature at  $3117$   
370  $\text{cm}^{-1}$  observed in liebermannite could be unrelated to stishovite, rather a spectral feature  
371 characteristic of liebermannite. We conclude that the similarities between liebermannite and stishovite  
372 may be related to similar substitution mechanisms of hydrogen in octahedral sites  $SiO_6$  or  $AlO_6$ .  
373 The preferential partitioning of water into the liebermannite phase over stishovite observed in our  
374 samples may be partly due to the low Al content in stishovite that is in equilibrium with

375 liebermannite (**Table 2**). Therefore, the presence of Al-free stishovite in the studied samples  
376 should not influence the IR spectra of liebermannite. Even in the case of very low water contents  
377 of about 16-30 wt. ppm observed in Al-free stishovite (Litasov et al., 2007), these should not affect  
378 water quantification of liebermannite in this study.

379

### 380 **4.3 Geophysical implications**

381 The upper mantle underneath the Philippine Sea (Tarits & Mandéa, 2010) and Northeastern  
382 China (Kelbert et al., 2009) is characterized by unusual electrical and seismic wave velocity  
383 structures, in particular, electrical conductivities as high as 1 S/m and high-velocity anomalies of  
384 up to  $+\delta V_P$  1.5 % and  $\delta V_S$  2.0 % have been observed in these regions. The observed anomalies  
385 cannot be readily explained by normal mantle consisting of major mantle phases such as olivine  
386 and wadsleyite (Manthilake et al., 2009). If the observed positive velocity anomalies were assumed  
387 to be caused by temperature variations alone, the temperature in the uppermost region of the mantle  
388 transition zone estimated to be about 800 K below the normal mantle geotherm (Manthilake et al.,  
389 2009). The corresponding electrical conductivity of hydrous olivine and wadsleyite for such low  
390 temperatures would be significantly lower; as a consequence, the proton conduction in olivine and  
391 wadsleyite cannot be responsible for the electrical conductivity observed at the upper mantle and  
392 in the mantle transition zone (Manthilake et al., 2009). Similarly, the presence of melt cannot  
393 explain the observed anomalies, because even a minor fraction of melt would significantly  
394 decrease both the primary ( $V_P$ ) and secondary ( $V_S$ ) wave velocities (Chantel et al., 2016; Freitas  
395 et al., 2017; Weidner et al., 2018).

396 Due to superionic conduction properties and high modal abundance ( $> 30$  vol. %) of  
397 liebermannite in deeply subducted crustal components, the electrical conduction in slabs is likely

398 to dominate by the liebermannite. This would make such slab components highly conductive  
399 compared to slabs consisting of mafic and ultramafic lithologies (Huang et al., 2005; Yoshino et  
400 al., 2008, 2008, 2014). However, the presence of liebermannite alone cannot account for the  
401 positive velocity anomaly observed in the upper mantle beneath the Philippine Sea (Tarits &  
402 Mandéa, 2010) and northeastern China (Kelbert et al., 2009) because the elastic wave velocities  
403 measured in liebermannite are comparable with those of common mantle mineral phases (Caracas  
404 & Boffa Ballaran, 2010; Mookherjee & Steinle-Neumann, 2009). Instead, the seismic wave  
405 velocities of Al-poor stishovite, another principal mineral phase stable in subducting continental  
406 sediments, are notably faster than those of mantle mineral phases (Gréaux et al., 2016). The  
407 stishovite co-existing with liebermannite in our samples is noticeably devoid of aluminum (**Table**  
408 **2**). Here we propose that Al-poor stishovite coexisting with liebermannite in the subducted  
409 continental sediments may be responsible for the positive velocity anomaly observed at the mantle  
410 transition zone beneath the Philippine Sea (Tarits & Mandéa, 2010) and northeastern China  
411 (Kelbert et al., 2009).

412 Continental crustal portion of the subducted slab, consisting of liebermannite, majoritic  
413 garnet, and stishovite, are expected to have a higher  $0.2 \text{ g cm}^{-3}$  density than the ambient mantle,  
414 but this density relation is overturned at the 660 km discontinuity (Irifune et al., 1994; Nishiyama  
415 et al., 2005). This implies that subducting crustal components of the slabs may penetrate into the  
416 mantle transition zone, but are prevented from entering the lower mantle (Nishiyama et al., 2005),  
417 such as those observed in the Northeastern China subduction system (Ichiki et al., 2006). However,  
418 the lower mantle origin of some of the plumes (French & Romanowicz, 2015; Hart et al., 1992)  
419 carrying the EM-type components in OIB magmas (Hart et al., 1992) provides strong evidence  
420 supporting the presence of recycled continental materials in the lower mantle. We propose that

421 mixing of continental with oceanic sediments may increase the density of sedimentary components  
422 facilitating the sinking of slabs towards the core-mantle boundary. The high electrical conductivity  
423 observed at a 1200 km depths in the Earth's lower mantle beneath the Philippine sea subduction  
424 system (Kelbert et al., 2009; Tarits & Mandéa, 2010) may be linked to such continuous subduction  
425 of continental sediments across the mantle transition zone into the Earth's lower mantle (**Fig. 7**).

426 Owing to hotter temperatures relative to the ambient mantle, the rising plume is unlikely  
427 to exchange incompatible elements, including water, with the surrounding mantle, including the  
428 hydrated MTZ and the upper mantle (Bercovici & Karato, 2003). Thus, it is likely that the H<sub>2</sub>O  
429 present in plume-derived rocks is primarily linked to the deep lower mantle source. The relatively  
430 high H<sub>2</sub>O contents of OIB derived from deep mantle plumes hint towards the presence of hydrated  
431 crustal components present in the deeper part of the lower mantle (**Fig. 8**). While major mineral  
432 phases in pyrolitic compositions are almost devoid of H<sub>2</sub>O under lower mantle conditions, our  
433 study demonstrates that liebermannite could be an important host of H<sub>2</sub>O in the Earth's lower  
434 mantle. In this scenario, H<sub>2</sub>O in the EMII-source OIB is primarily related to deeply subducted  
435 continental materials, in which liebermannite is the principal H<sub>2</sub>O carrier. On the other hand, the  
436 subducted continental materials that may reach the core-mantle boundary would hydrate the HIMU  
437 type plume sources together with a possible contribution from *dense hydrous magnesium silicates*  
438 (DHMS) (Nishi et al., 2014; Pamato et al., 2014) and primordial H<sub>2</sub>O (Dixon et al., 2002).

439

440

441

442

443

444 **Acknowledgments**

445 We thank Nathalie Bolfan-Casanova and Maud Boyet for constructive discussion, J-L. Devidal for  
446 his assistance with electron microprobe analyses and Emmy Voyer for her assistance with SEM  
447 analyses. The constructive and in-depth reviews by the associate Editor, and two reviewers: Lidong  
448 Dai and Hongzhan Fei substantially improved the quality of the manuscript. G.M. acknowledges  
449 funding from the(INSU-CNRS. M.M. is supported by the US National Science Foundation grants,  
450 EAR 1753125, 1763215. This research was financed by the French Government Laboratory of  
451 Excellence initiative n°ANR-10-LABX-0006, the Région Auvergne, and the European Regional  
452 Development Fund (ClerVolc contribution number xx). The authors comply with AGU's data  
453 policy, and the data of this study are available in Figshare.

454 ([https://figshare.com/articles/Water\\_content\\_calculations/12179067](https://figshare.com/articles/Water_content_calculations/12179067))

455 and ([https://figshare.com/articles/Experimental\\_data\\_xlsx/12179046](https://figshare.com/articles/Experimental_data_xlsx/12179046)).

456 The authors declare no competing financial interests.

457

458 **References**

459 Bercovici, D., & Karato, S.-I. (2003). Whole-mantle convection and the transition-zone water  
460 filter. *Nature*, *425*(6953), 39–44. <https://doi.org/10.1038/nature01918>

461 Bethell, D. E., & Sheppard, N. (1953). The Infrared Spectrum of the H<sub>3</sub>O<sup>+</sup> Ion in Acid  
462 Hydrates. *Journal of Chemical Physics*, *21*, 1421. <https://doi.org/10.1063/1.1699260>

463 Bolfan-Casanova, N., Keppler, H., & Rubie, D. C. (2003). Water partitioning at 660 km depth  
464 and evidence for very low water solubility in magnesium silicate perovskite. *Geophysical*  
465 *Research Letters*, *30*(17), 1905. <https://doi.org/10.1029/2003GL017182>

466 Cabral, R. A., Jackson, M. G., Koga, K. T., Rose-koga, E. F., Hauri, E. H., Whitehouse, M. J., et

- 467 al. (2014). Volatile cycling of H<sub>2</sub>O, CO<sub>2</sub>, F, and Cl in the HIMU mantle: A new window  
468 provided by melt inclusions from oceanic hot spot lavas at Mangaia, Cook Islands.  
469 *Geochemistry Geophysics Geosystems*, 15, 4445–4467.  
470 <https://doi.org/10.1002/2014GC005473>.Received
- 471 Caracas, R., & Boffa Ballaran, T. (2010). Elasticity of (K,Na)AlSi<sub>3</sub>O<sub>8</sub> hollandite from lattice  
472 dynamics calculations. *Physics of the Earth and Planetary Interiors*, 181(1–2), 21–26.  
473 Retrieved from <http://dx.doi.org/10.1016/j.pepi.2010.04.004>
- 474 Chantel, J., Manthilake, G., Andrault, D., Novella, D., Yu, T., & Wang, Y. (2016). Experimental  
475 evidence supports mantle partial melting in the asthenosphere. *Science Advances*, 2(5),  
476 e1600246.
- 477 Cynn, H., & Hofmeister, A. M. (1994). High-pressure IR spectra of lattice modes and OH  
478 vibrations in Fe-bearing wadsleyite. *Journal of Geophysical Research*, 99(B9), 17717–  
479 17727. <https://doi.org/10.1029/94jb01661>
- 480 Deschamps, F., Kaminski, E., & Tackley, P. J. (2011). A deep mantle origin for the primitive  
481 signature of ocean island basalt. *Nature Geoscience*, 4(11), 1–4.  
482 <https://doi.org/10.1038/ngeo1295>
- 483 Dixon, J. E., Leist, L., Langmuir, C., & Schilling, J. (2002). Recycled dehydrated lithosphere  
484 observed in plume-influenced mid-ocean-ridge basalt. *Nature*, 420, 385–389.
- 485 Fei, H., Druzhbin, D., & Katsura, T. (2020). The Effect of Water on Ionic Conductivity in  
486 Olivine. *Journal of Geophysical Research: Solid Earth*, 125(3).  
487 <https://doi.org/10.1029/2019JB019313>
- 488 Ferroir, T., Onozawa, T., Yagi, T., Merkel, S., Miyajima, N., Nishiyama, N., et al. (2006).  
489 Equation of state and phase transition in KAlSi<sub>3</sub>O<sub>8</sub> hollandite at high pressure. *American*

- 490 *Mineralogist*, 91, 327–332. <https://doi.org/10.2138/am.2006.1879>
- 491 Freitas, D., & Manthilake, G. (2019). Electrical conductivity of hydrous silicate melts :  
492 Implications for the bottom-up hydration of Earth ' s upper mantle. *Earth and Planetary*  
493 *Science Letters*, 523, 115712. <https://doi.org/10.1016/j.epsl.2019.115712>
- 494 Freitas, D., Manthilake, G., Schiavi, F., Chantel, J., Bolfan-Casanova, N., Bouhifd, M. A., &  
495 Andraut, D. (2017). Experimental evidence supporting a global melt layer at the base of the  
496 Earth's upper mantle. *Nature Communications*, 8(1), 2186. [https://doi.org/10.1038/s41467-](https://doi.org/10.1038/s41467-017-02275-9)  
497 [017-02275-9](https://doi.org/10.1038/s41467-017-02275-9)
- 498 French, S. W., & Romanowicz, B. (2015). Broad plumes rooted at the base of the Earth's mantle  
499 beneath major hotspots. *Nature*, 525(7567), 95–99. <https://doi.org/10.1038/nature14876>
- 500 Fu, S., Yang, J., Karato, S. ichiro, Vasiliev, A., Presniakov, M. Y., Gavriiliuk, A. G., et al.  
501 (2019). Water Concentration in Single-Crystal (Al,Fe)-Bearing Bridgmanite Grown From  
502 the Hydrous Melt: Implications for Dehydration Melting at the Topmost Lower Mantle.  
503 *Geophysical Research Letters*, 46(17–18), 10346–10357.  
504 <https://doi.org/10.1029/2019GL084630>
- 505 Furusawa, S., Suemoto, T., & Ishigame, M. (1988). Quasielastic light scattering in the one-  
506 dimensional superionic conductor hollandites. *Physical Review B*, 38(17), 12600–12606.
- 507 Gréaux, S., Kono, Y., Wang, Y., Yamada, A., Zhou, C., Jing, Z., et al. (2016). Sound velocities  
508 of aluminum-bearing stishovite in the mantle transition zone. *Geophysical Research Letters*,  
509 43, 4239–4246. <https://doi.org/10.1002/2016GL068377>.Received
- 510 Hacker, B. R. (2008). H2O subduction beyond arcs. *Geochemistry Geophysics Geosystems*, 9(3),  
511 Q03001. <https://doi.org/10.1029/2007GC001707>
- 512 Hart, S. R. (1988). Heterogeneous mantle domains : signatures , genesis and mixing

- 513 chronologies. *Earth and Planetary Science Letters*, 90, 273–296.
- 514 Hart, S. R., Hauri, E. H., Oschmann, L. A., & Whitehead, J. A. (1992). Mantle Plumes and  
515 Entrainment : Isotopic Evidence. *Science*, 256, 517–521.
- 516 He, Y., Sun, Y., Lu, X., Gao, J., Li, H., & Li, H. (2016). First-principles prediction of fast  
517 migration channels of potassium ions in KAlSi<sub>3</sub>O<sub>8</sub> hollandite: Implications for high  
518 conductivity anomalies in subduction zones. *Geophysical Research Letters*, 43(12), 6228–  
519 6233. <https://doi.org/10.1002/2016GL069084>.Received
- 520 van der Hilst, R. D., Widiyantoro, S., & Engdahl, E. R. (1997). Evidence for deep mantle  
521 circulation from global tomography. *Nature*, 386, 578–584. Retrieved from  
522 <http://dx.doi.org/10.1038/386578a0>
- 523 Hirschmann, M. M. (2006). Water, Melting, and the Deep Earth H<sub>2</sub>O Cycle. *Annual Review of*  
524 *Earth and Planetary Sciences*, 34(1), 629–653.  
525 <https://doi.org/10.1146/annurev.earth.34.031405.125211>
- 526 Hu, H., Li, H., Dai, L., Shan, S., & Zhu, C. (2013). Electrical conductivity of alkali feldspar solid  
527 solutions at high temperatures and high pressures. *Physics and Chemistry of Minerals*,  
528 40(1), 51–62. <https://doi.org/10.1007/s00269-012-0546-4>
- 529 Huang, X., Xu, Y., & Karato, S. (2005). Water content in the transition zone from electrical  
530 conductivity of wadsleyite and ringwoodite. *Nature*, 434(7034), 746–749.  
531 <https://doi.org/10.1038/nature03426>
- 532 Ichiki, M., Baba, K., Obayashi, M., & Utada, H. (2006). Water content and geotherm in the  
533 upper mantle above the stagnant slab : Interpretation of electrical conductivity and seismic  
534 P-wave velocity models. *Physics of the Earth and Planetary Interiors*, 155, 1–15.  
535 <https://doi.org/10.1016/j.pepi.2005.09.010>

- 536 Irifune, T., Ringwood, A. E., & Hibberson, W. O. (1994). Subduction of continental crust and  
537 terrigenous and pelagic sediments: an experimental study. *Earth and Planetary Science*  
538 *Letters*, *126*, 351–368.
- 539 Katsura, T., Sato, K., & Ito, E. (1998). Electrical conductivity of silicate perovskite at lower-  
540 mantle conditions. *Nature*, *395*(October), 493–495. <https://doi.org/10.1038/26736>
- 541 Katsura, T., Yoneda, A., Yamazaki, D., Yoshino, T., Ito, E., Suetsugu, D., et al. (2010).  
542 Adiabatic temperature profile in the mantle. *Physics of the Earth and Planetary Interiors*,  
543 *183*(1–2), 212–218. <https://doi.org/10.1016/j.pepi.2010.07.001>
- 544 Kawai, K., & Tsuchiya, T. (2013). First-principles study on the high-pressure phase transition  
545 and elasticity of  $\text{KAlSi}_3\text{O}_8$  hollandite. *American Mineralogist*, *98*, 207–218.  
546 <https://doi.org/10.2138/am.2007.2246>
- 547 Kelbert, A., Schultz, A., & Egbert, G. (2009). Global electromagnetic induction constraints on  
548 transition-zone water content variations. *Nature*, *460*(7258), 1003–1006.  
549 <https://doi.org/10.1038/nature08257>
- 550 Khanna, S. K., Gruner, G., Orbach, R., & Beyeler, H. U. (1981). Thermally Activated  
551 Microwave Conductivity in the Superionic Conductor Hollandite  
552 ( $\text{K}_{1.54}\text{Mg}_{0.77}\text{Ti}_{7.23}\text{O}_{16}$ ). *Physical Review Letters*, *47*(4), 255–257.
- 553 Koch-Müller, M., & Rhede, D. (2010). IR absorption coefficients for water in nominally  
554 anhydrous high-pressure minerals. *American Mineralogist*, *95*(5–6), 770–775.  
555 <https://doi.org/10.2138/am.2010.3358>
- 556 Litasov, K. D., Kagi, H., Shatskiy, A., Ohtani, E., Lakshtanov, D. L., Bass, J. D., & Ito, E.  
557 (2007). High hydrogen solubility in Al-rich stishovite and water transport in the lower  
558 mantle. *Earth and Planetary Science Letters*, *262*, 620–634.

- 559 <https://doi.org/10.1016/j.epsl.2007.08.015>
- 560 Manthilake, G., Matsuzaki, T., Yoshino, T., Yamashita, S., Ito, E., & Katsura, T. (2009).  
561 Electrical conductivity of wadsleyite as a function of temperature and water content.  
562 *Physics of the Earth and Planetary Interiors*, 174(1–4), 10–18.  
563 <https://doi.org/10.1016/j.pepi.2008.06.001>
- 564 Manthilake, G., Mookherjee, M., Bolfan-Casanova, N., & Andraut, D. (2015). Electrical  
565 conductivity of lawsonite and dehydrating fluids at high pressures and temperatures.  
566 *Geophysical Research Letters*, 42(18), 7398–7405. <https://doi.org/10.1002/2015GL064804>
- 567 Miura, H. (1986). The crystal structure of hollandite. *Mineralogical Journal*, 13(3), 119–129.
- 568 Mookherjee, M., & Steinle-Neumann, G. (2009). Detecting deeply subducted crust from the  
569 elasticity of hollandite. *Earth and Planetary Science Letters*, 288(3–4), 349–358.  
570 <https://doi.org/10.1016/j.epsl.2009.09.037>
- 571 Ni, H., Keppler, H., Manthilake, M. A. G. M., & Katsura, T. (2011). Electrical conductivity of  
572 dry and hydrous NaAlSi<sub>3</sub>O<sub>8</sub> glasses and liquids at high pressures. *Contributions to*  
573 *Mineralogy and Petrology*, 162(3), 501–513. <https://doi.org/10.1007/s00410-011-0608-5>
- 574 Nishi, M., Irifune, T., Tsuchiya, J., Tange, Y., Nishihara, Y., Fujino, K., & Higo, Y. (2014).  
575 Stability of hydrous silicate at high pressures and water transport to the deep lower mantle.  
576 *Nature Geoscience*, 7, 224–227. <https://doi.org/10.1038/NGEO2074>
- 577 Nishiyama, N., Rapp, R. P., Irifune, T., Sanehira, T., Yamazaki, D., & Funakoshi, K. I. (2005).  
578 Stability and P – V – T equation of state of KAlSi<sub>3</sub>O<sub>8</sub> -hollandite determined by in situ X-  
579 ray observations and implications for dynamics of subducted continental crust material.  
580 *Physics and Chemistry of Minerals*, 32, 627–637. <https://doi.org/10.1007/s00269-005-0037->  
581 y

- 582 Ohta, K., Hirose, K., Ichiki, M., Shimizu, K., Sata, N., & Ohishi, Y. (2010). Electrical  
583 conductivities of pyrolitic mantle and MORB materials up to the lowermost mantle  
584 conditions. *Earth and Planetary Science Letters*, 289(3–4), 497–502.  
585 <https://doi.org/10.1016/j.epsl.2009.11.042>
- 586 Pamato, M. G., Myhill, R., Boffa Ballaran, T., Frost, D. J., Heidelbach, F., & Miyajima, N.  
587 (2014). Lower-mantle water reservoir implied by the extreme stability of a hydrous  
588 aluminosilicate. *Nature Geoscience*, 8, 75–79. <https://doi.org/10.1038/NGEO2306>
- 589 Rodriguez-Carvajal, J. (1993). Recent advances in magnetic structure determination by neutron  
590 powder diffraction. *Physica B: Condensed Matter*, 192, 55–69.
- 591 Schiavi, F., Bolfan-Casanova, N., Withers, A. C., Médard, E., Laumonier, M., Laporte, D., et al.  
592 (2018). Water quantification in silicate glasses by Raman spectroscopy: Correcting for the  
593 effects of confocality, density and ferric iron. *Chemical Geology*, 483(March), 312–331.  
594 <https://doi.org/10.1016/j.chemgeo.2018.02.036>
- 595 Schmidt, M. W. (1996). Experimental Constraints on Recycling of Potassium from Subducted  
596 Oceanic Crust. *Science*, 272(5270), 1927–1930.  
597 <https://doi.org/10.1126/science.272.5270.1927>
- 598 Sinmyo, R., Pesce, G., Greenberg, E., McCammon, C., & Dubrovinsky, L. (2014). Lower mantle  
599 electrical conductivity based on measurements of Al, Fe-bearing perovskite under lower  
600 mantle conditions. *Earth and Planetary Science Letters*, 393, 165–172.  
601 <https://doi.org/10.1016/j.epsl.2014.02.049>
- 602 Smyth, J. R., & Jacobsen, S. D. (2006). Nominally anhydrous minerals and Earth ' s deep water  
603 cycle. (S. van der Lee & S. D. Jacobsen, Eds.), *American Geophysical Union Monograph*  
604 *Series*. Washington DC: American Geophysical Union.

- 605 Sueda, Y., Irifune, T., Nishiyama, N., Rapp, R. P., Ferroir, T., Onozawa, T., et al. (2004). A new  
606 high-pressure form of  $\text{KAlSi}_3\text{O}_8$  under lower mantle conditions. *Geophysical Research*  
607 *Letters*, *31*(23), 1–4. <https://doi.org/10.1029/2004GL021156>
- 608 Syracuse, E. M., Keken, P. E. Van, Abers, G. A., van Keken, P. E., Abers, G. A., Suetsugu, D.,  
609 et al. (2010). The global range of subduction zone thermal models. *Physics of the Earth and*  
610 *Planetary Interiors*, *183*(1–2), 73–90. <https://doi.org/10.1016/j.pepi.2010.02.004>
- 611 Tarits, P., & Mandéa, M. (2010). The heterogeneous electrical conductivity structure of the  
612 lower mantle. *Physics of the Earth and Planetary Interiors*, *183*, 115–125.  
613 <https://doi.org/10.1016/j.pepi.2010.08.002>
- 614 Urakawa, S., Kondo, T., Igawa, N., Shimomura, O., & Ohno, H. (1994). Synchrotron Radiation  
615 Study on the High-Pressure and High-Temperature Phase Relations of  $\text{KAlSi}_3\text{O}_8$ . *Physics*  
616 *and Chemistry of Minerals*, *21*, 387–391.
- 617 Weidner, D. J., Li, L., Whitaker, M. L., & Triplett, R. (2018). Ultrasonic Acoustic Velocities  
618 During Partial Melting of a Mantle Peridotite KLB-1. *Journal of Geophysical Research:*  
619 *Solid Earth*, *123*(2), 1252–1261. <https://doi.org/10.1002/2017JB014753>
- 620 Willbold, M., & Stracke, A. (2006). Trace element composition of mantle end-members:  
621 Implications for recycling of oceanic and upper and lower continental crust. *Geochemistry*  
622 *Geophysics Geosystems*, *7*, Q04004. <https://doi.org/10.1029/2005GC001005>
- 623 Yoshikado, S., Ohachi, T., Taniguchi, I., Onoda, Y., Watanabe, M., & Fujiki, Y. (1982). Ionic  
624 conductivity of hollandite type compounds from 100 Hz to 37.0 GHz. *Solid State Ionics*, *7*,  
625 335–344.
- 626 Yoshino, T., Manthilake, G., Matsuzaki, T., & Katsura, T. (2008). Dry mantle transition zone  
627 inferred from the conductivity of wadsleyite and ringwoodite. *Nature*, *451*(7176), 326–329.

628 <https://doi.org/10.1038/nature06427>

629 Yoshino, T., Nishi, M., Matsuzaki, T., Yamazaki, D., & Katsura, T. (2008). Electrical  
630 conductivity of majorite garnet and its implications for electrical structure in the mantle  
631 transition zone. *Physics of the Earth and Planetary Interiors*, 170(3–4), 193–200.

632 <https://doi.org/10.1016/j.pepi.2008.04.009>

633 Yoshino, T., Shimojuku, A., & Li, D. (2014). Electrical conductivity of stishovite as a function  
634 of water content. *Physics of the Earth and Planetary Interiors*, 227, 48–54.

635 <https://doi.org/10.1016/j.pepi.2013.12.003>

636 Yoshino, T., Kamada, S., Zhao, C., Ohtani, E., & Hirao, N. (2016). Electrical conductivity model  
637 of Al-bearing bridgmanite with implications for the electrical structure of the Earth's lower  
638 mantle. *Earth and Planetary Science Letters*, 434, 208–219.

639 <https://doi.org/10.1016/j.epsl.2015.11.032>

640

641

642

643

644

645

646

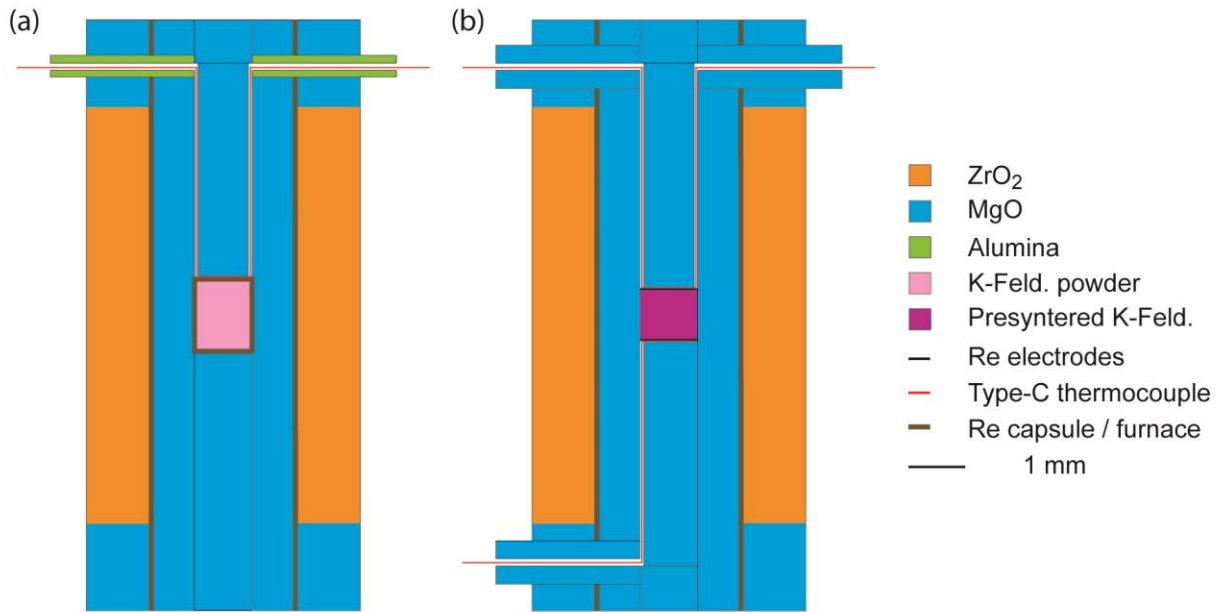
647

648

649

650

651 **Figures**



652

653 **Fig.1. A schematic cross-section of the assembly. (a) Used for the synthesis of K-feldspar. (b)**

654 **For electrical conductivity measurements at high-pressure and high-temperature. The three-**

655 **electrode configuration for electrical conductivity, which designed to avoid electrode leads sharing**

656 **the same tungsten carbide anvil in the KAWAI-cell, is expected to improve the insulation**

657 **resistance of the assembly.**

658

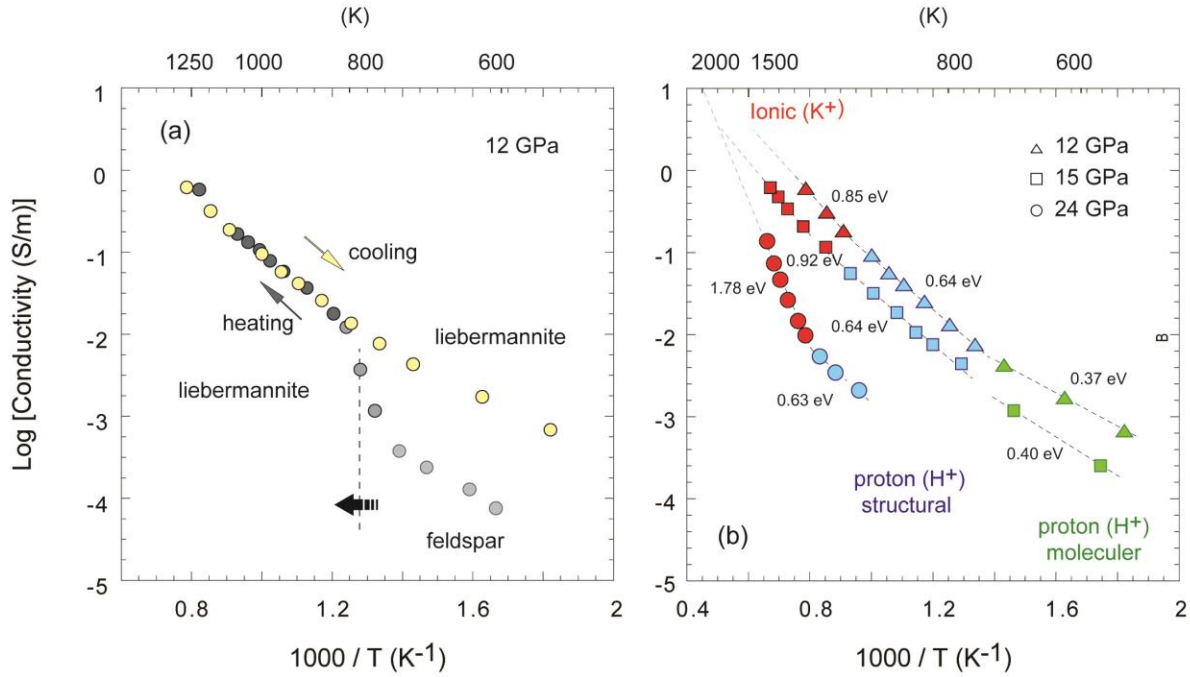
659

660

661

662

663



664

665 **Fig. 2. The electrical conductivity of liebermannite as a function of inverse temperature. (a)**

666 A plot of the logarithm of electrical conductivity as a function of inverse temperature. The

667 transformation of K-feldspar to liebermannite occurred above 600 K resulting in more than one

668 order of magnitude increase of conductivity. (b) Liebermannite at pressures 12, 15, and 24 GPa.

669 Different conduction mechanisms are labeled in different colors. The activation enthalpies are

670 shown next to individual fitting lines. The error bars associated with the electrical conductivity

671 data measurements are less than the symbol size at high temperatures.

672

673

674

675

676

677  
 678  
 679  
 680  
 681  
 682  
 683  
 684  
 685  
 686  
 687  
 688  
 689  
 690  
 691  
 692  
 693  
 694  
 695  
 696  
 697  
 698  
 699

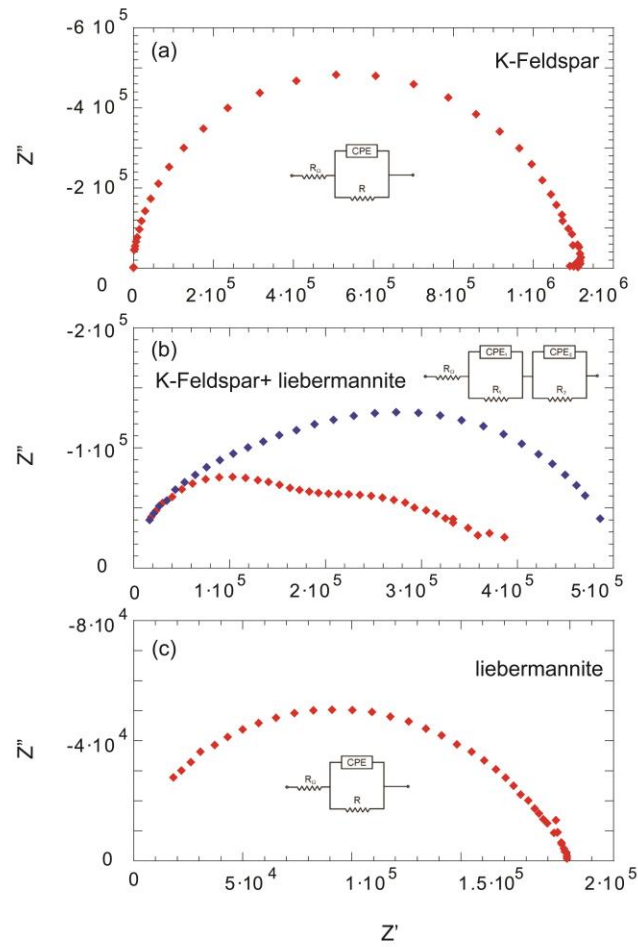


**Fig. 3.** Impedance spectra of the sample at different stages of heating at 12 GPa. (a) at 500 K electrical conductivity of K-feldspar before transforming into liebermannite, (b) at 718 K and 750 K, on the onset of the phase transformation, the second arc in the spectra develops. These additional arcs correspond to the formation of liebermannite. (c) At 850 K, after the complete transformation into liebermannite, there is a significant increase in the sample resistance. The sample resistance is due to the single conductive liebermannite phase. The corresponding equivalent circuit.

700  
701  
702  
703  
704  
705  
706  
707  
708  
709  
710  
711  
712  
713  
714  
715  
716  
717  
718  
719  
720  
721  
722

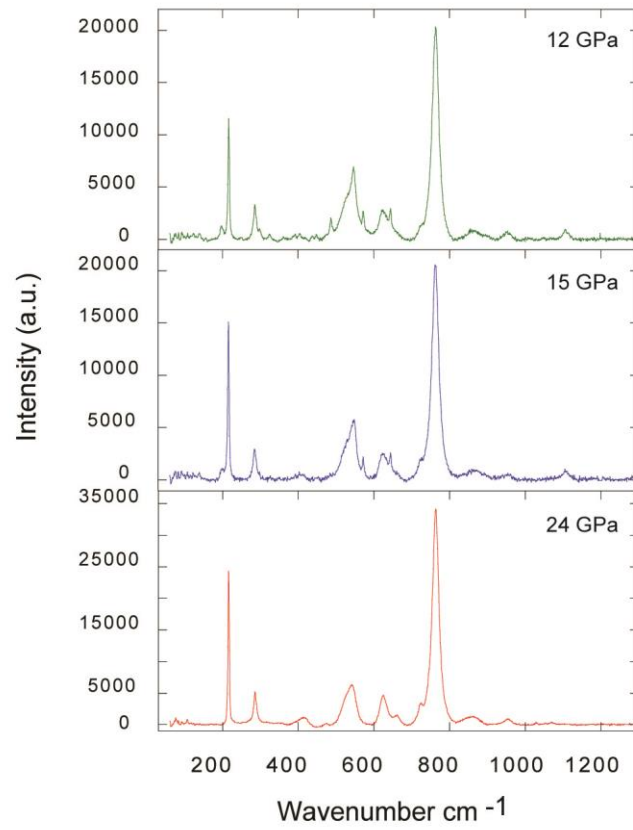


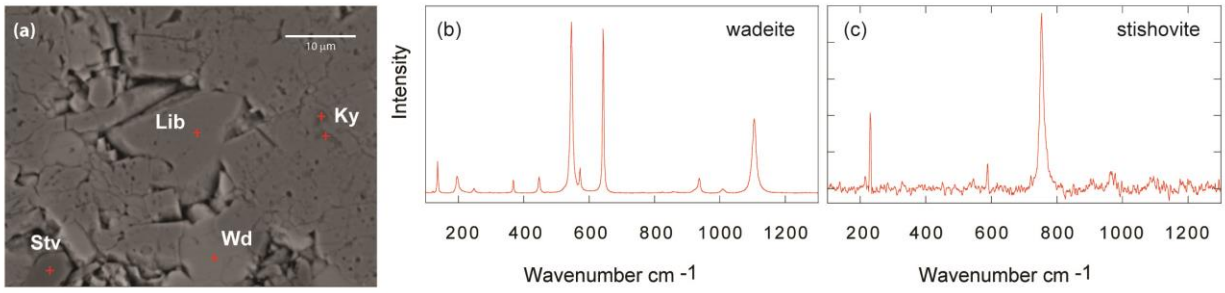
**Fig. 4.** Raman spectra of liebermannite at 12, 15, and 24 GPa.

723

724

725

726



727

728 **Fig. 5. Mineral assemblages of the recovered sample.** (a) A back-scattered electron image

729 showing the mineral assemblage at 15 GPa. (b, c) Low-wavenumber bands corresponding to

730 vibrations of the alumino-silicate network; (b) wadeite, (c) stishovite.

731

732

733

734

735

736

737

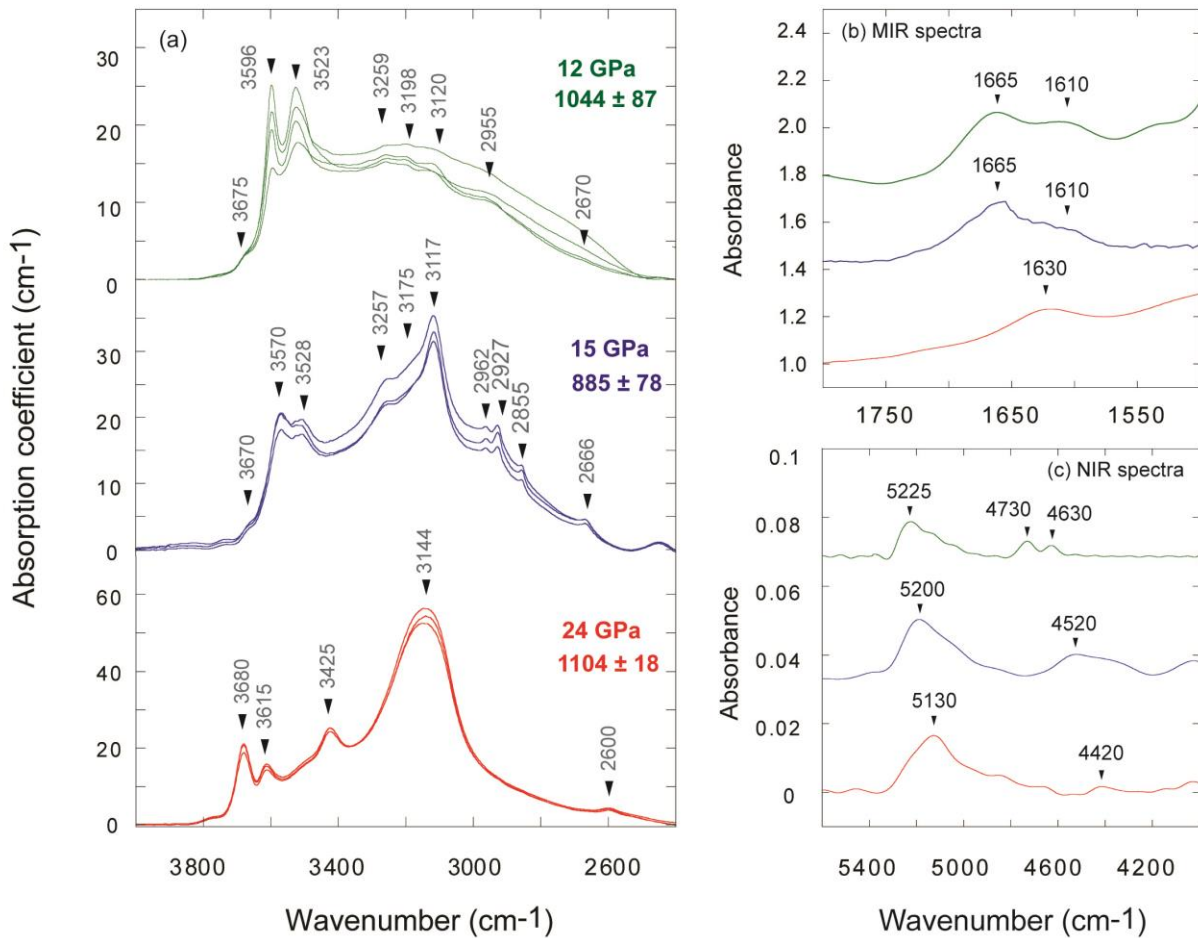
738

739

740

741

742



743

744

745

746 **Fig. 6. FTIR spectra of liebermannite.** (a) Near IR spectra of samples synthesized at 12 (green  
 747 lines), 15 (blue lines), and 24 (red lines) GPa. The calculated H<sub>2</sub>O contents (ppm wt.) are indicated  
 748 next to spectra. (b) Middle IR spectra of the three samples showing bending modes of H<sub>2</sub>O  
 749 molecules and H<sub>3</sub>O<sup>+</sup> ions. (c) High-wavenumber IR region displaying bands at ~5200 (stretching  
 750 vibrations of H<sub>2</sub>O) and 4500-4700 cm<sup>-1</sup> (O-H stretching vibrations). The peak at 4170 cm<sup>-1</sup> could  
 751 be related to H-H vibrations.

752  
753  
754  
755  
756  
757  
758  
759  
760  
761  
762  
763  
764  
765  
766  
767  
768  
769  
770  
771  
772  
773  
774

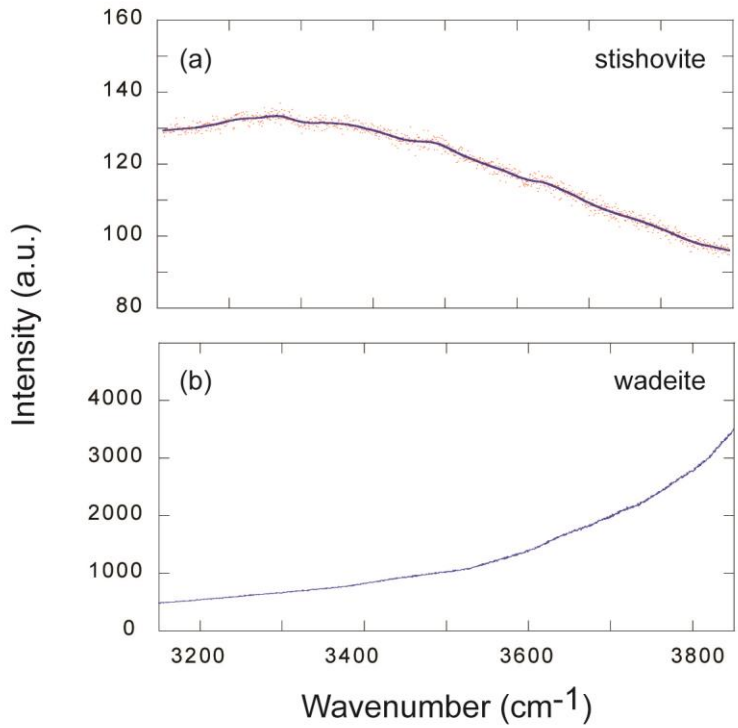


**Fig. 7. Raman spectra of minor phases observed at the sample synthesized at 15 GPa.** The background uncorrected Raman spectra in the O-H region of stishovite (a) and wadeite (b), co-existing with liebermannite. The background noise of the Raman spectrum of stishovite was smoothed using the loess regression method shown in the blue line. Both indicate water absent conditions in their crystal structure. Raman analyses of kyanite were not possible due to their small grain sizes.

775  
776  
777  
778  
779  
780  
781  
782  
783  
784  
785  
786  
787  
788  
789  
790  
791  
792  
793  
794  
795  
796  
797  
798

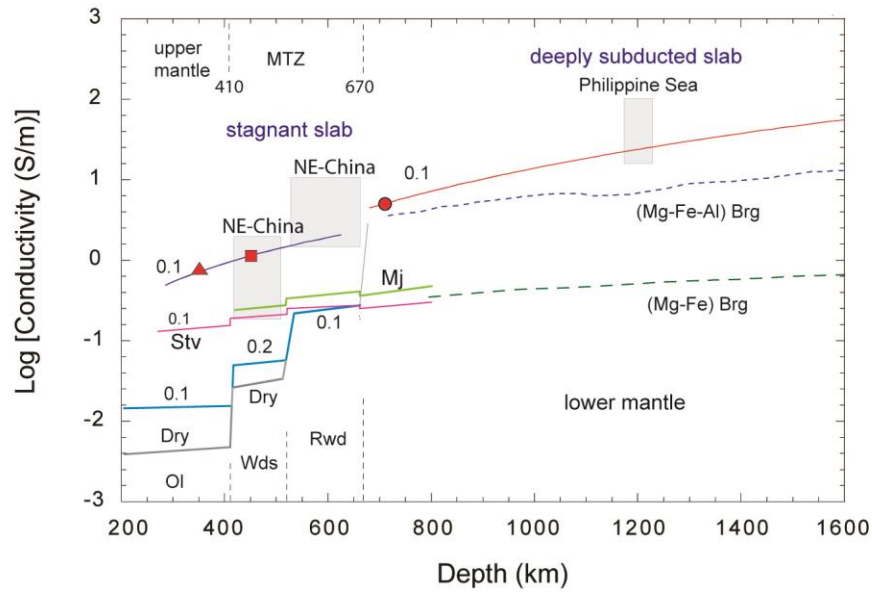
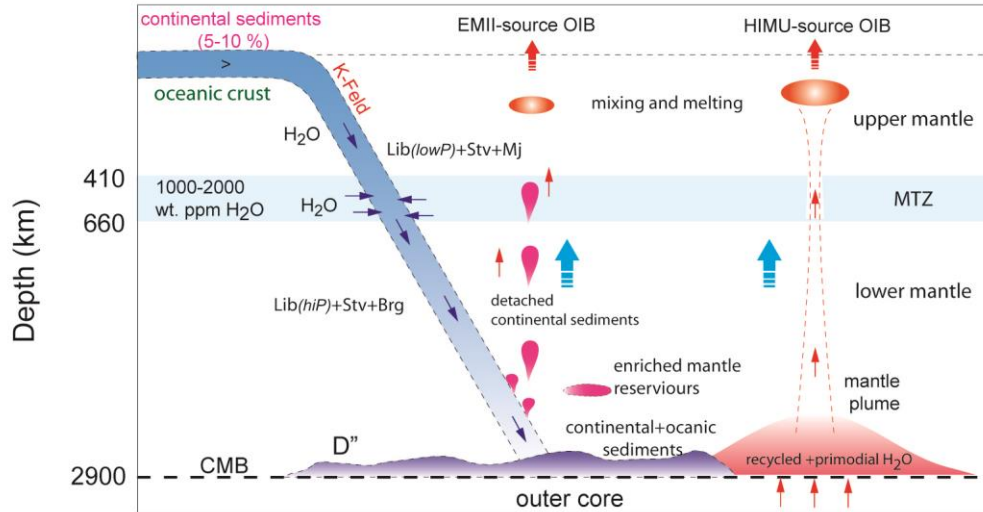


**Fig. 8. Comparison of electrical conductivities of liebermannite with global and regional electrical conductivity profiles.** The blue and red lines correspond to the extrapolation of electrical conductivity along the relevant subduction geotherms (Syracuse et al., 2010), and along the adiabatic geotherm in the lower mantle (Katsura et al., 2010), respectively. The red shaded triangle, square, and the circle indicate the electrical conductivity of liebermannite at 12, 15, and 24 GPa, respectively. The gray shaded boxes indicate the conductivity profiles of NE-China (Kelbert et al., 2009) and the Philippine Sea (Tarits & Mandéa, 2010). The electrical conductivity profiles of dry (black lines) and wet (blue lines) olivine, wadsleyite, ringwoodite (Yoshino et al., 2008), stishovite with 0.1 wt% of H<sub>2</sub>O (Yoshino et al., 2014) (pink lines) and majorite garnet (Yoshino et al., 2008) (light green lines) are shown for comparison. The electrical conductivity of (Mg, Fe) bridgmanite (Katsura et al., 1998) (green dashed line) and (Mg, Fe, Al) bridgmanite (Ohta et al., 2010; Sinmyo et al., 2014; Yoshino et al., 2016) (blue dashed line), extrapolated along the adiabatic geotherm in the lower mantle (Katsura et al., 2010), are shown for comparison. The numbers next to conductivity lines are the water contents in wt. %.

799  
800  
801  
802  
803  
804  
805  
806



807 **Fig. 9. The potential mechanism explaining the elevated H<sub>2</sub>O content in ocean island basalts.**

808 K-feldspar in subducting continental sediments transforms to liebermannite above 8 GPa and  
 809 continues to be stable down to the core-mantle boundary conditions. Most of the H<sub>2</sub>O carried to  
 810 the lower mantle by deep penetrating slabs may have been incorporated into the slab at the surface.  
 811 However, due to the imbalance of the mass of H<sub>2</sub>O transported to the Mantle Transition Zone  
 812 (MTZ) via subduction (Hacker, 2008) and the estimated mass of H<sub>2</sub>O stored in MTZ based on  
 813 H<sub>2</sub>O contents of constituent phases (Freitas & Manthilake, 2019), extraction of H<sub>2</sub>O from MTZ  
 814 to the lower mantle can be expected. Because of the ability of liebermannite to accommodate several  
 815 wt. % of the water in its structure (both in lattice defects and the tunnel structures), we argue that  
 816 liebermannite could be a possible carrier of water from the MTZ to the lower mantle. In this two-  
 817 step, H<sub>2</sub>O conveyor process, the extraction of H<sub>2</sub>O by rehydration of deep penetrating slabs at the  
 818 MTZ would be a likely scenario. Depending on gravitational stability, the subducting continental  
 819 sediment component may detach from deep-extending slabs, rise through the mantle forming  
 820 EMII-source OIB, in which liebermannite is the principal water carrier. Some continental  
 821 sediments may reach the CMB and provide H<sub>2</sub>O for HIMU-source lower mantle-derived plumes.  
 822 (Lib: liebermannite, Sa: K-feldspar, Mj: majorite garnet, Brg: bridgmanite, Stv; stishovite).

823  
824  
825

826 **List of tables**

827

**Table 1.** The reference pre-exponential factor  $\text{Log } \sigma_0$  and the activation enthalpy in eV for liebermannite at 12, 15, and 24 GPa and their respective water contents.

Pressure (GPa)	Temperature (K)	Log $\sigma_0$ *	Log $\sigma_0$ **	$\Delta H$ *	$\Delta H$ **	H <sub>2</sub> O contents ppm wt.
12	550 -750	0.57	n.a	0.37	n.a.	1044 ± 87
	750 - 1100	2.19	2.32	0.64	0.78	
	>1100	3.14	3.88	0.85	0.82	
15	573 - 683	0.58	n.a	0.4	n.a.	885 ± 78
	773 -1173	1.76	1.61	0.64	0.76	
	> 1173	2.78	3.96	0.92	0.83	
24	1040 - 1200	0.38	0.24	0.63	0.76	1104 ± 18
	> 1270	5	8.26	1.78	0.89	

\* parameters from individual fitting

\*\* parameters from single fit

n.a: not nalyzed

828

829 **Table 2.** Chemical composition of the constituent mineral phases.

830

831

832

833

834

835

836

837

838

839

840

841

842

843

844

845

846

847

848

849

**Table 2.** Chemical composition of the constituent mineral phases.

	Liebermannite			Wadeite		Stishovite		Kyanite	
	12 GPa	15 GPa	24 GPa	12 GPa	15 GPa	12 GPa	15 GPa	12 GPa	15 GPa
<b>SiO<sub>2</sub></b>	64.44 (0.7)	63.91 (2.5)	66.70 (0.2)	73.00 (0.9)	71.82 (0.5)	100.50 (0.8)	101.13 (0.5)	38.23 (0.9)	39.11 (0.9)
<b>K<sub>2</sub>O</b>	16.47 (0.4)	16.18 (1.2)	16.42 (1.8)	27.16 (0.8)	28.22 (0.6)	0.06 (0.3)	0.13 (0.07)	0.15 (0.06)	0.61 (0.4)
<b>Al<sub>2</sub>O<sub>3</sub></b>	18.98 (0.3)	20.4 (2.9)	17.21 (2.0)	0.15 (0.1)	0.6 (0.5)	0.05 (0.2)	0.07 (0.03)	62.6 (1.2)	61.35 (1.2)
<b>Total</b>	<b>99.89</b>	<b>100.49</b>	<b>100.33</b>	<b>100.31</b>	<b>100.64</b>	<b>100.62</b>	<b>101.33</b>	<b>100.98</b>	<b>101.07</b>

The standard deviation indicated in parenthesis.

850